ENGINEERING

Phenotypic targeting using magnetic nanoparticles for rapid characterization of cellular proliferation regulators

Zongjie Wang[1,2], Hansen Wang[2], Sichun Lin[2,3], Stephane Angers[2,3], Edward H. Sargent[4,5,6,7], Shana O. Kelley[1,2,4,5,7,8,9,10]*

Genome-wide CRISPR screens have provided a systematic way to identify essential genetic regulators of a phenotype of interest with single-cell resolution. However, most screens use live/dead readout of viability to identify factors of interest. Here, we describe an approach that converts cell proliferation into the degree of magnetization, enabling downstream microfluidic magnetic sorting to be performed. We performed a head-to-head comparison and verified that the magnetic workflow can identify the same hits from a traditional screen while reducing the screening period from 4 weeks to 1 week. Taking advantage of parallelization and performance, we screened multiple mesenchymal cancer cell lines for their dependency on cell proliferation. We found and validated pan- and cell-specific potential therapeutic targets. The method presented provides a nanoparticle-enabled approach means to increase the breadth of data collected in CRISPR screens, enabling the rapid discovery of drug targets for treatment.

INTRODUCTION

Uncontrolled expansion and invasion are essential characteristics of cancer cells (*1*). Targeting the division of cancer cells has been proven to be an effective strategy for cancer therapy. For example, many mainstream chemotherapies induce DNA damage and slow the proliferation of malignant cells (*2*), achieving remarkable long-term remission in many types of cancers (*3*). However, the intrinsic stemness and heterogeneity within cancer cell populations promote the development of drug resistance and continued to proliferate through various mechanisms (*4*, *5*), such as dissemination (*6*), epithelial-to-mesenchymal transition (*7*, *8*), and metastasis (*9*). Therefore, it is essential to gain a comprehensive understanding of the proliferation landscape of cancer cells, especially for the metastatic phenotypes that drive cancer progression.

The development of CRISPR-Cas9 has revolutionized biological research by enabling on-demand adaption, expression, and interference of specific genes (*10*). CRISPR-Cas9–mediated whole-genome screening has enabled pooled loss-of-function genetic screens with high resolution and genome-wide coverage (*11*) and led to the discovery of multiple sets of genes defining the landscape of important biological processes, including cell fitness (*11*), drug resistance (*12*), and immune evasion (*13*). In such screens, a large number of cancer cells (>50 million per replicate) are transfected with a pooled library and cultured for a long period, typically 2 to 4 weeks, to allow a viability phenotype to be preferentially enriched (*11*, *13*). Although sorting cells based on a specific molecular marker may help to accelerate the screening process (*14*), it is very challenging to use fluorescence-activated cell sorting (FACS) to process a large number of cells due to its limited throughput (*15*). Moreover, FACS commonly loses 50 to 70% of input cells due to bad droplet formation or incorrect scanning (*16*, *17*). Such a loss in desired phenotypes is likely to depress the quality of the screen and hinder the interpretation of hits.

We recently introduced microfluidic immunomagnetic cell sorting (MICS) as an alternative to FACS (*15*, *18*, *19*). MICS used antibodies conjugated with magnetic nanoparticles (MNPs) to label a specific surface marker and separate labeled cells by their degree of magnetization through a microfluidic system; therefore, it offers a single-cell resolution during profiling (*20*). Compared to FACS, MICS has notable advantages in throughput (up to 10^8 cells in an hour) and led to the successful discovery of the regulator for CD47 (*15*). In addition to surface markers, MICS is compatible with intracellular markers (*21*) and messenger RNA (*22*) within fixed and permeabilized cells and has enabled the tracking of disease-associated mutations/phenotypes in a noninvasive liquid biopsy manner (*21–23*). However, phenotypic processes, such as cell proliferation, are complicated and many of them are not measurable by just labeling a single RNA or protein marker. Therefore, there remains a need to develop a magnetic assay for the MICS system to extend its applicability in highly complex phenotypic screens.

Here, we describe an approach to measure cell proliferation using nanoparticle-mediated magnetization—the Nanomagnetic Proliferation (NanoPro) assay. The NanoPro assay relies on the internalization, maintenance, and separation of intracellular MNPs during cell proliferation. We demonstrate that the NanoPro assay has comparable performance and less cell stress compared to traditional proliferation assay. We show that the integration of a NanoPro and MICS system provides a fast, low-cost, ultrahigh-throughput means to sort highly proliferative cells from bulk populations. With the help of NanoPro and MICS, we performed genome-wide CRISPR screens on four highly metastatic mesenchymal human cancer cell lines and found a core gene set defining the proliferation

[1]Department of Biomedical Engineering, McCormick School of Engineering, Northwestern University, Evanston, IL 60208, USA. [2]Department of Pharmaceutical Sciences, Leslie Dan Faculty of Pharmacy, University of Toronto, Toronto M5S 3M2, Canada. [3]Terrence Donnelly Centre for Cellular & Biomolecular Research, University of Toronto, Toronto M5S 3E1, Canada. [4]The Edward S. Rogers Sr. Department of Electrical & Computer Engineering, University of Toronto, Toronto M5S 3G4, Canada. [5]Department of Chemistry, Weinberg College of Arts and Science, Northwestern University, Evanston, IL 60208, USA. [6]Department of Electrical and Computer Engineering, McCormick School of Engineering, Northwestern University, Evanston, IL 60208, USA. [7]International Institute for Nanotechnology, Northwestern University, Evanston, IL 60208, USA. [8]Robert H. Lurie Comprehensive Cancer Center, Northwestern University, Chicago, IL 60611, USA. [9]Simpson Querrey Institute, Northwestern University, Chicago, IL 60611, USA. [10]Chan Zuckerberg Biohub Chicago, Chicago, IL 60607, USA.

*Corresponding author. Email: shana.kelley@northwestern.edu

landscape and revealing pan- and cell-specific potential therapeutic targets.

RESULTS

Design and validation of the NanoPro assay

The current gold standard compound for quantitating cell proliferation is carboxyfluorescein succinimidyl ester (CFSE), which is cell permeable and covalently coupled to intracellular lysine residue via its succinimidyl group (24). CFSE emits bright green fluorescence and is divided equally between daughter cells, making it an optimal candidate for tracking the number of cell divisions in a fixed time frame via flow cytometry (25). We noticed that the small nanoparticles (<40 nm) internalized by the cells share similar characteristics compared to CFSE, including rapid uptake (26–28) and stable maintenance in the cytoplasm with very limited externalization (29, 30) and equal separation between daughter cells during cell division (29). In addition, small nanoparticles are reported to have no effect on proliferation and viability at a dose of 0.1 nM in the short term (31, 32). This provides a rationale to examine the utility of small MNPs as a means to convert the efficiency of proliferation into the degree of magnetization (Fig. 1A).

We examined the cellular uptake behavior of 25-nm MNPs functionalized with a Cyanine 5 (Cy5) reporter on the surface using MDA-MB-231, a human triple-negative breast cancer cell line. We first confirmed the biocompatibility of the MNPs through calcein AM staining and methoxynitrosulfophenyl-tetrazolium carboxanilide (XTT) assays and did not observe significant changes in viability, apoptosis, and proliferation rate up to the concentration of 100 µg ml^{-1} (Fig. 1B and fig. S1, C and D); this matches well with the toxicity study of MNPs reported before (33). The uptake of MNPs occurred in the first 8 hours of incubation (fig. S1A), and the number of internalized MNPs is linear to the concentration of dosage in the range from 1 to 100 µg/ml (fig. S1B). Confocal microscopy revealed that the MNPs were mainly distributed in the cytoplasm (Fig. 1C and fig. S2A) and split during mitosis into two daughter cells. We also quantified the density of internalized MNPs during 4 days of culture by flow cytometry (Fig. 1D); the reduction of fluorescence intensity follows Gaussian distribution and is exponential to the day of culture (coefficient = −0.734), suggesting that the separation of MNPs is relatively uniform over multiple divisions. It is worth noting that the linearity of the MNP assay is comparable to the gold standard CFSE labeling (fig. S2B; both >0.99). In addition, direct quantitation of internalized MNPs by transmission electron microscopy (TEM) reveals a similar trend; the coverage of MNPs decreased exponentially over the 5 days of culture (coefficient = −0.684, $R^2 > 0.999$). We previously identified the doubling time of MDA-MB-231 as 24 hours (34), which yields a coefficient of −0.693. The well-matched coefficients from the MNP density and cell proliferation curve indicate that the separation of internalized 25-nm MNPs is uniform and closely related to the number of mitoses. Besides, we validated the trafficking behavior (fig. S2C), fixability (fig. S2D), and generality (over different cell lines; fig. S2E) of the MNPs and found that the performance is comparable to the CFSE assay. The only noticeable difference is that CD4$^+$ T cells were better stained by CFSE rather than by NanoPro. This is likely due to the TCR (T cell receptor)–based mechanism that T cells use to uptake nanoparticles (35). We also monitored the MNP density in a slowly proliferating cell line, SH-SY5Y [doubling time, 67.3 ± 5.8 hours (36)]. On the basis of

fluorescence signals, we believe that the MNPs were retained within the cytoplasm of SH-SY5Y cells for at least 11 days (fig. S2F), suggesting the long-term stability and usability of MNPs. Together, we believe that the use of 25-nm MNPs is as efficient as CFSE for tracking cell proliferation, as summarized in table S1. This approach is able to convert the potency of proliferation into the degree of magnetization, enabling the downstream magnetic sorting to be performed.

Design and characterization of magnetic sorting system

The design of the NanoPro assay enabled us to adopt our microfluidic magnetic sorting system for separating cells based on the efficiency of proliferation. Our microfluidic sorting approach is based on the degree of magnetization (Fig. 2A). In brief, cells labeled by different levels of MNPs were introduced into a microfluidic device that is attached to permanent magnets. With the magnetic field generated by the magnets, cells labeled with a certain number of MNPs would acquire enough magnetic force to compensate for the fluidic drag force. As a result, the cell labeled by more MNPs (equivalent to the cells with lower potency of proliferation in the case of NanoPro) can tolerate a higher flow rate and remain in the high-velocity zone. Considering the exponential decay of MNP loading during proliferation, we believe that previous designs featuring linear changes in fluidic drag forces are not well suited for the NanoPro assays (37). Therefore, we have developed a different design that consists of four distinct thicknesses (100, 200, 400, and 800 µm; fig. S3, A and B), which yields to 100, 50, 25, and 12.5%, respectively, of the normalized fluidic velocity or fluidic drag force (fig. S3). Considering this, the device is designed to offer a sorting profile wherein the cells captured in the subsequent zone will undergo one additional division compared to those in the previous zone. Using NanoPro-labeled MDA-MB-231 cells, we optimized the sorting conditions to 5 ml/hour, which allows most cells to be captured in zones 1, 2, and 3 on days 2, 3, and 4, respectively (fig. S4). The optimal flow rate for NanoPro is substantially lower than the condition we reported previously for antibody-mediated sorting (10 to 30 ml/hour) (37) due to the use of MNPs with a smaller size (25 versus 50 nm). It is worth mentioning that large nanoparticles (>100 nm) are reported to split asymmetrically during cell division (38, 39). Hence, we did not explore the opportunity to use nonmicrofluidic approaches or microparticles for sorting NanoPro-labeled cells.

We next quantified the performance of two distinct systems for sorting cells based on their proliferation (CFSE with FACS and NanoPro with MICS; Fig. 2, B and C). CFSE/MNP-labeled cells (CFSE$^+$/MNP$^+$) were mixed with unlabeled cells (CFSE$^-$/MNP$^-$) in equal fractions to serve as the raw material for platform characterization and benchmarking. Notably, MICS achieved a throughput of 50 to 100 million cells/hour per device when running at an optimal flow of 5 ml/hour and a concentration of 10 to 20 million cells/ml and therefore offered a 10- to 50-fold higher throughput compared to FACS. FACS and MICS achieved similar sorting purity overall. For cancer cells prone to clumping like MDA-MB-231, MICS offered better purity in the positive fraction than FACS likely because of its speed, which limits cell aggregation. On the other hand, however, we consistently observed a significant difference between the cell recovery of FACS and MICS; MICS yields a 2- to 4-fold higher cell recovery compared to FACS. This is not an unexpected result as FACS can lose up to 70% of input cells due to bad droplet formation or incorrect scanning (16, 17). In addition, for aggregation-prone
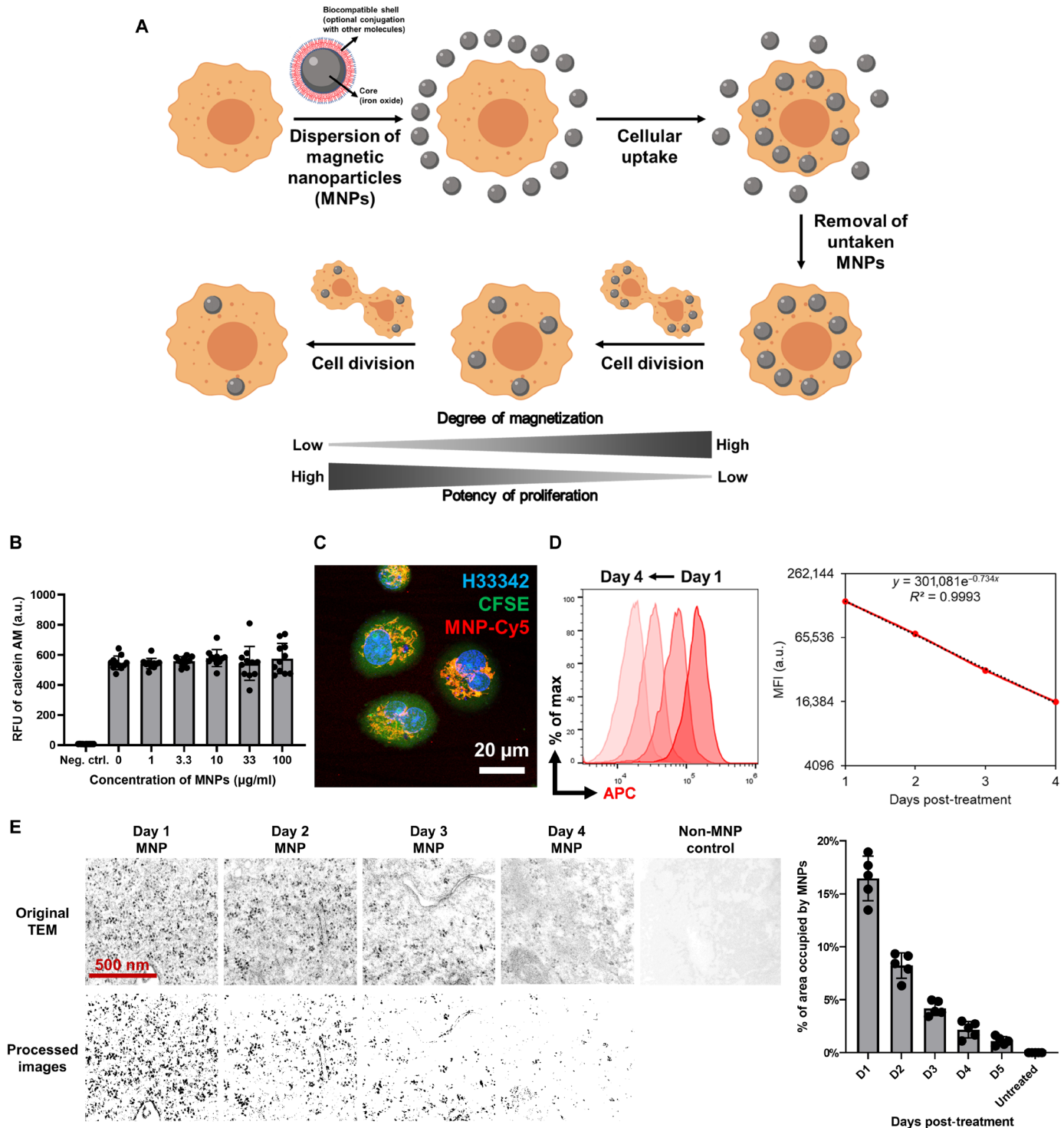
Fig. 1. NanoPro assay to convert cell proliferation into a magnetic gradient. (**A**) Workflow of the NanoPro assay. MNPs were internalized by cells and divided equally during the cell division process, which converts the potency of proliferation into degree of magnetic labeling. (**B**) Quantitation of the cell viability after MNP internalization. No significant difference was observed. (**C**) Confocal images of live cells with internalized MNPs. MNPs were distributed in the cytoplasm with no noticeable leakage to the extracellular region. (**D**) Quantitation of the linearity of MagPro assays. MNP-internalized cells were monitored for four consecutive days for its median fluorescence intensity (MFI). A coefficient of 0.9993 was achieved when linear regression was applied. (**E**) Representative TEM images and quantitation of the internalized MNPs. The number of beads decreased exponentially, matching the proposed mechanism and flow cytometric data.
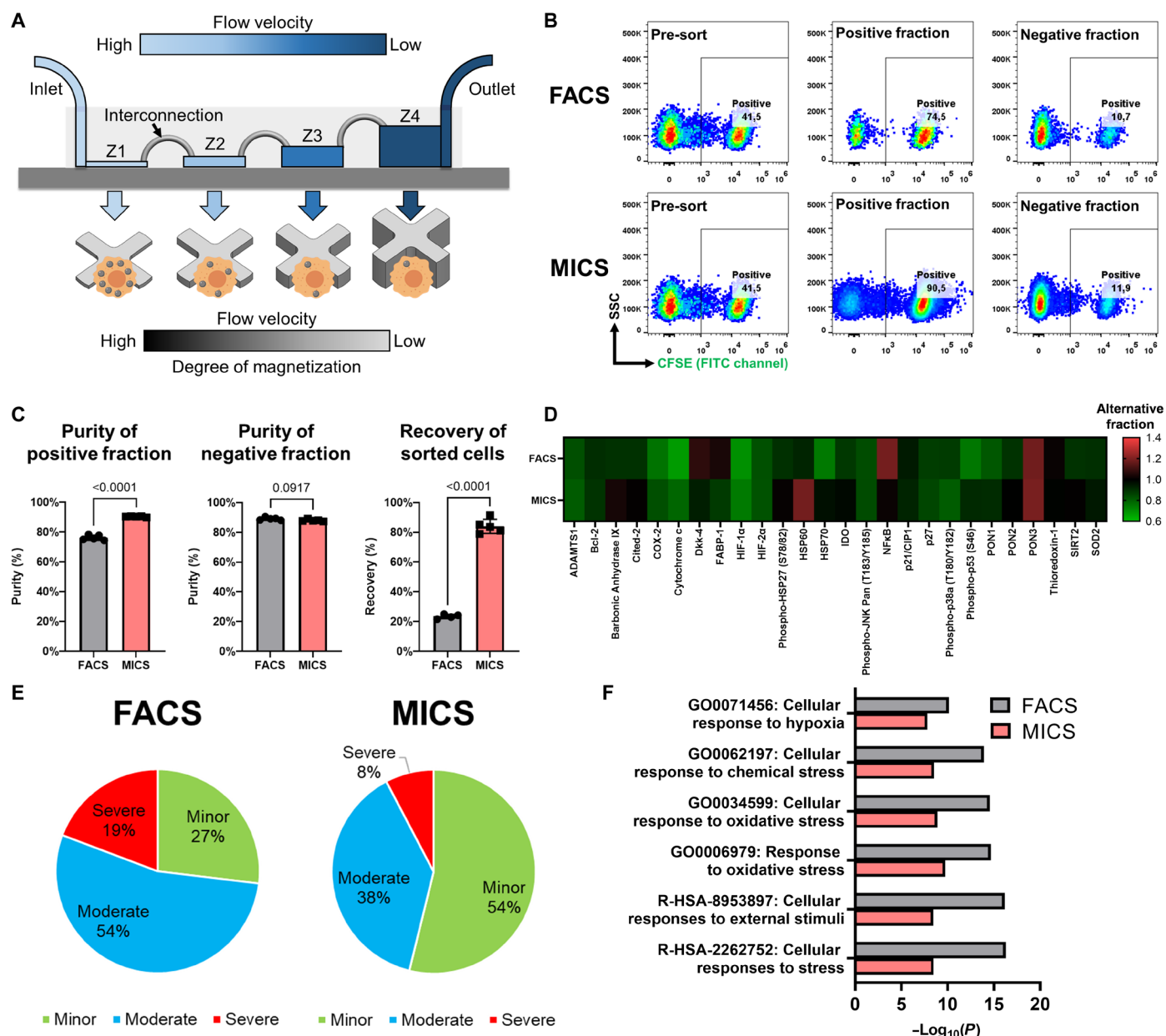
Fig. 2. MICS system to enable high-throughput and gentle sorting of cells based on the degree of magnetic labeling. (**A**) Working principle of the MICS system realized by microfluidic chips with different thicknesses. (**B**) Representative cytometric profile of pre- and post-sort MDA-MB-231 cells by the FACS and MICS system. The pre-sort MDA-MB-231 cells contain two pre-generated and mixed populations (CFSE$^+$/MNP$^+$ and CFSE$^-$/MNP$^-$) for benchmarking purposes. (**C**) Quantitation of purity and recovery of sorting. (**D**) Heatmap of the protein expression of cell stress markers after sorting, normalized to unsorted controls. (**E**) Summary of cell stress profile after sorting. Minor, moderate, and severe changes are defined as the variation with 10%, 10 to 20%, and >20% compared to unsorted control, respectively. (**F**) ORA results of common cell stress pathways using moderately and severely changed phosphorylated proteins.

cells, FACS is required to perform cell resuspension/filtration frequently, which contributes to excessive cell loss.

Given that functional genomic screens will report on any stress exerted on CRISPR-edited cells, we investigated cell stress generated during sorting by surveying the phosphorylation of 26 common stress-related markers (Fig. 2D and fig. S5). Notably, in FACS-sorted samples, shear stress–related markers, such as COX-2 (*40*) and HSP70 (*41*), were significantly altered. This alteration was not observed in MICS-sorted samples (Fig. 2E) likely due to its extremely low shear

stress (<0.5 Pa according to simulation) (*42*). This result matches well with the previous studies suggesting that FACS can generate significant changes in the phosphorylation (*43*) and metabolome (*44*) of sorted cells when applying the hydrodynamic force and shear stress for proper sorting. We observed sufficiently lower enrichment of stress-related pathways in MICS compared to FACS during overrepresentation analysis (ORA; Fig. 2F). However, it is noteworthy that, although MICS imposes low shear stress on sorted cells, oxidative stress–related markers, such as hypoxia-inducible factor–1α (HIF-1α)

(*45*) and cytochrome c (*46*), were still severely affected by both MICS and FACS procedures. There is still room to further optimize the sorting protocol to reduce oxidative stress on the cells.

Together, MICS offers better performance over FACS in terms of throughput, cell recovery, and cell stress, as summarized in table S2. Compared to other microfluidic cell sorting platforms, such as cell size–based sorting, the combination of NanoPro and MICS offers a first-of-its-kind sorting based on the ability of proliferation (refer to table S3 for comparison). Microfluidic sorting based on cell proliferation is highly complementary to existing sorting schemes based on protein expression (*47*, *48*) and cell size/deformability (*49*, *50*). Together, these technologies may offer a more holistic approach for analyzing the effects of genetic perturbations on cell phenotypes.

NanoPro for genome-wide proliferative screen

Having demonstrated the feasibility of NanoPro and MICS for sorting cells based on their proliferation, we next benchmarked the hits from different approaches using MDA-MB-231 cells carrying genome-wide knockouts generated by transfecting the Toronto KnockOut (TKOv3

library (*11*). The workflow is shown in Fig. 3A. Wild-type cells were first transfected by lentivirus carrying genome-wide coverage of single-guide RNAs (sgRNAs) on a Cas9-expressing backbone at a multiplicity of infection (MOI) of 0.3, followed by a 48-hour selection of puromycin. CRISPRed cells were split and labeled by NanoPro or CFSE. Labeled cells were cultured for another 4 to 5 days to allow three to four rounds of division. In the end, cells were sorted by MICS or FACS. Sorted highly proliferative populations (NanoPro^{low} or CFSE^{low}) and unsorted controls were sequenced for sgRNA enrichment and analysis. It is noteworthy that, for the CRISPR screen process, we used regular 25-nm MNPs without Cy5 labeling due to their cost-effectiveness.

We first determined the quality of the screen carried by NanoPro/MICS with the internal negative control sgRNAs in TKOv3 targeting luciferase, green fluorescent protein (GFP), and LacZ, which are not expressed in human cell lines and therefore would not generate any impact on proliferation. Ranking of sgRNAs through the Bayesian Analysis of Gene Essentiality (BAGEL) algorithm (*51*) reveals that the negative control genes, including *luc2* (luciferase), *GFP*, and
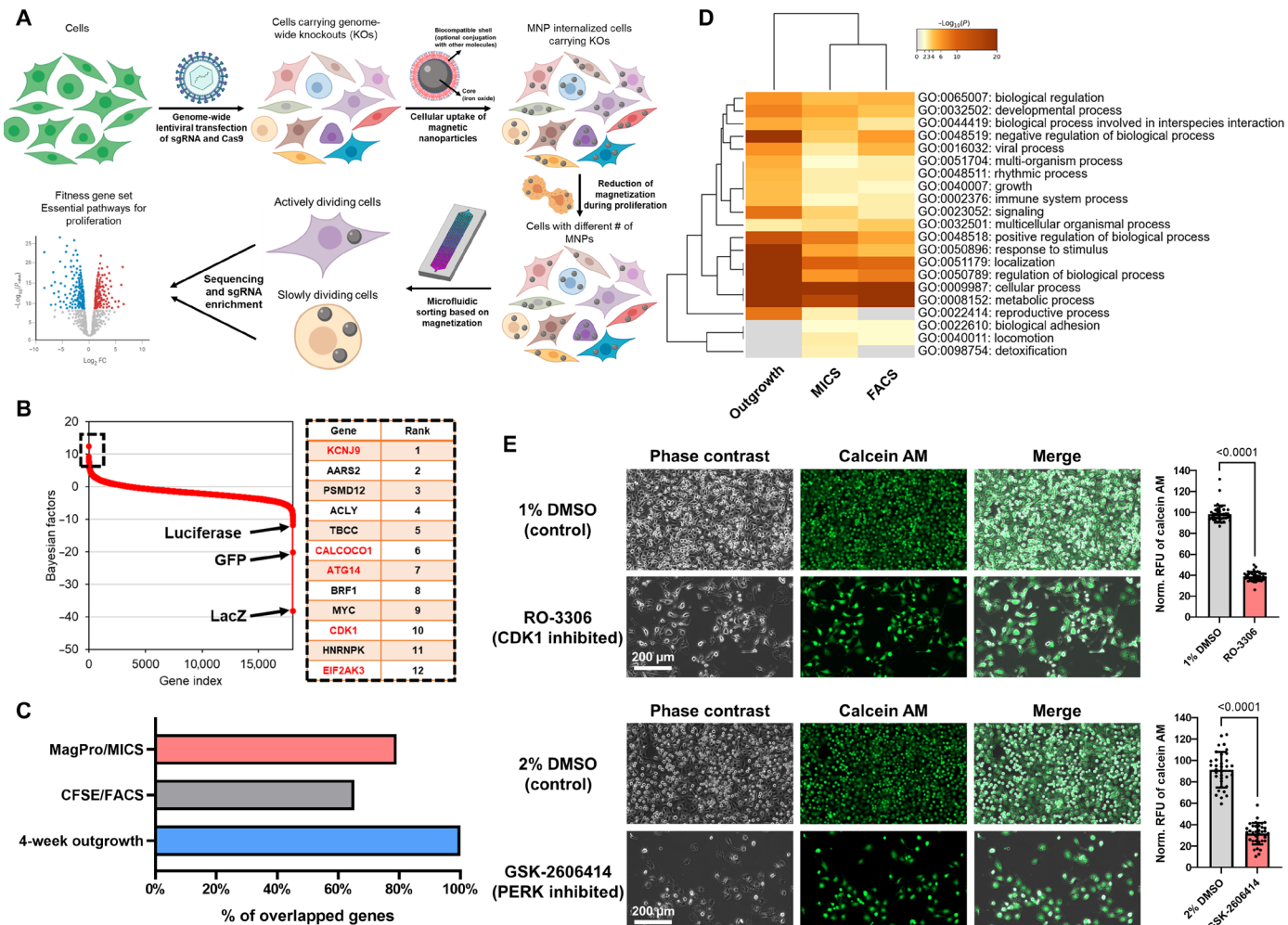

Fig. 3. NanoPro and MICS enable genome-wide screen on the proliferation of MDA-MB-231 cells. (**A**) Workflow of the genome-wide screen of cell proliferation using the NanoPro assay and MICS. (**B**) Rank of essential genes for proliferation calculated by the BAGEL algorithm. The red fonts indicate the noncommon genes reported for proliferation. (**C**) Comparison of the percentage of overlapped hits from different ways/replicates of the screen. (**D**) Pathway enrichment among the hits from different ways/replicates of the screen. (**E**) Validation of the druggable top hits (*CDK1* and *PERK*) from the screen by corresponding inhibitors.

lacZ, are the last three sgRNAs in the gene rank (Fig. 3B), indicating that they are least relevant to cell proliferation. In addition, we examined the sgRNA distribution of our top hits and confirmed a significant deduction when comparing sorted to unsorted populations (fig. S6). Not surprisingly, 7 of 10 top hits (Fig. 3B) are reported before as common genes affecting cell proliferation (*11*). Together, the location of negative controls and the enrichment of previously identified genes in top hits confirm that the screen carried by NanoPro/MICS is of good quality.

Using the recommended standard of false discovery rate (FDR) < 0.3 and Bayes factor (BF) > 2, we identified gene sets that regulate the proliferation of MDA-MB-231 cells from different approaches and compare their overlap (Fig. 3C). NanoPro/MICS successfully recovered 80% of genes presenting in the traditional, 4-week-long outgrowth screen, whereas CFSE/FACS can only recover about 65%. This is likely due to the cell loss during sorting that dims the difference among sgRNAs or the biased amplification during the excessive rounds of polymerase chain reaction (PCR) to prepare libraries from recovered sgRNAs for sequencing (*52*). We also performed an ORA using the gene sets with the gene ontology; all approaches yield a similar profile of enrichment (Fig. 3D). Together, this head-to-head comparison shows that the NanoPro/MICS workflow yields a better screen result than the CFSE/FACS workflow. Eighty percent of the hits in the 4-week-long traditional screen can also be identified in the 1-week-long NanoPro/MICS workflow; this results in a fourfold faster turnaround and helps to reduce the reagent cost up to 75%.

To examine the effectiveness of the top hits from the NanoPro/MICS workflow, we picked two druggable hits: *CDK1* and *EIF2AK3* (also known as *PERK*). By adding corresponding inhibitors during culture, we observed a significant decrease (>50%) in proliferation in vitro (Fig. 3E). It is worth noting that the slowly growing cells still exhibit high levels of viability; this means that NanoPro/MICS has the ability to discriminate hits that relate to proliferation versus those resulting from essential genes.

Core proliferation gene set of mesenchymal cancers

Having demonstrated the quality and rapidness of the NanoPro/MICS workflow for screening cell proliferation, we next used this approach to probe the proliferation landscape of mesenchymal cancer cells. Mesenchymal phenotypes are with a strong ability to migrate and therefore often form metastasis on a remote organ (*53*). In addition, mesenchymal phenotypes often established a less immunogenic tumor microenvironment that limits the outcome of immunotherapy (*54*). Hence, understanding the proliferation landscape of mesenchymal cancer cells would provide insights into therapeutic modalities. With the aim to build a pan-cancer landscape, we picked four mesenchymal cell lines obtained from different cancer types: MDA-MB-231 for breast cancer, SBC5 for small cell lung cancer, SK-MEL-5 for melanoma, and HeLa for cervical cancer, as shown in Fig. 4A.

We first confirmed their mesenchymal phenotypes by running Western blotting of epithelial (E-cadherin) and mesenchymal (vimentin) hallmarks (Fig. 4B). Compared to the epithelial cancer cells (e.g., MCF-7), our panel of mesenchymal cells consistently displayed vimentin$^+$E-cadherin$^-$ phenotypes. Subsequently, we used the NanoPro/MICS workflow presented in Fig. 3A and performed the proliferation screen. Notably, these mesenchymal cell lines are of similar sizes (15 to 20 μm in diameter) and exhibit similar MNP uptake

profiles (fig. S2E). Therefore, we applied the same sorting flow rate (5 ml/hour) determined from the MDA-MB-231 cell line to all cell lines. After sorting, highly proliferative cells were collected for sequencing and BAGEL analyses. To obtain the data for analysis, two to three biological replicates of screens were performed for each cell line. In each biological replicate, four or more sgRNAs were used to target a specific gene. The statistical cutoff for identifying hits was set as follows: an FDR of less than 0.3 and a BF score greater than 2, as recommended by the BAGEL algorithm. Hits from different cell lines were compared (Fig. 4C and fig. S7), and the hits presented in multiple cell lines were considered as core proliferation gene sets (Fig. 4D). In total, 530 genes were identified (see the Supplementary Materials). Only six of the genes are shared by all cell lines: *TRRAP*, *RPL30*, *PSMD6*, *RCL1*, *TUBB*, and *ZBTB11*.

We investigated genes specific to individual cell lines to assess their impact on proliferation (Fig. 4, E to G, and fig. S8). We studied the impact of five druggable genes from the core set: *PRODH*, *MMP7*, *MCT1*, *FURIN*, and *TUBB*. We found that the reduction of proliferation (Fig. 4E and fig. S8A), as measured by the total fluorescence signals of viable cells, is highly associated with the screen results (Fig. 4F). In addition to measuring the fluorescence intensity, we stained the treated MDA-MB-231 cells with Ki-67 to confirm the reduction of proliferation at the molecular level (fig. S8B). Furthermore, we stained the treated MDA-MB-231 cells with annexin V and confirmed that the drug treatment resulted in minor changes of apoptosis (<10%; fig. S8C). These observations demonstrate the validity of the NanoPro-mediated CRISPR screens. We noticed a potential dependency between hits and mutations in the targeted genes as two cell lines with *TP53* mutations (MDA-MB-231 and SBC5) are sensitive to pan-MMP and FURIN inhibition (Fig. 4F). The increased dependency of *TP53*-mutant cells on pan-MMP and FURIN inhibition might explain recent observations that multiple *TP53*-mutant cells had significantly up-regulated expression of *MMP*s (*55*) and were sensitive to *MMP7*-targeting antiproliferation treatment (*56*). Together, these results highlight the utility of data derived from NanoPro screens for the discovery of mutation-specific treatments. However, additional screens and biological assays are necessary to further unravel the relationship among *MMP*s and *FURIN* and cell proliferation in *TP53*-mutant cells.

We next studied the enrichment of pathways in the panel of cell lines (Fig. 4, G and H). ORA among common pathway databases results in 400 to 600 significantly enriched pathways for each cell line (Fig. 4G). Here, 242 pathways are enriched in all cell lines, suggesting that the proliferation of mesenchymal cancer cells shares a substantial portion of common pathways. In addition to the 242 shared pathways, each cell line has 60 to 133 unique pathways showing their individualized dependency on pathways. We further plotted the shared common pathways as the heatmap of gene ratio and $-\log_{10}(P)$ (Fig. 4H). Most pathways are related to DNA synthesis, RNA processing, RNA splicing, cell cycle advancement, and mitotic separation; all of these pathways are critical processes during cell division (*57*). In addition to the general pathways, unexpected pathways were also enriched, such as the regulation of slit guidance ligands and roundabout homologs (SLIT/ROBO), and the TCF (T cell factor)–dependent signaling. This indicates that the mesenchymal cancer cells may commonly use specific pathways for maintaining their invasiveness and proliferation.

In addition to the cell line–specific pathways, we also considered the core gene sets as a whole for analysis to yield more general and
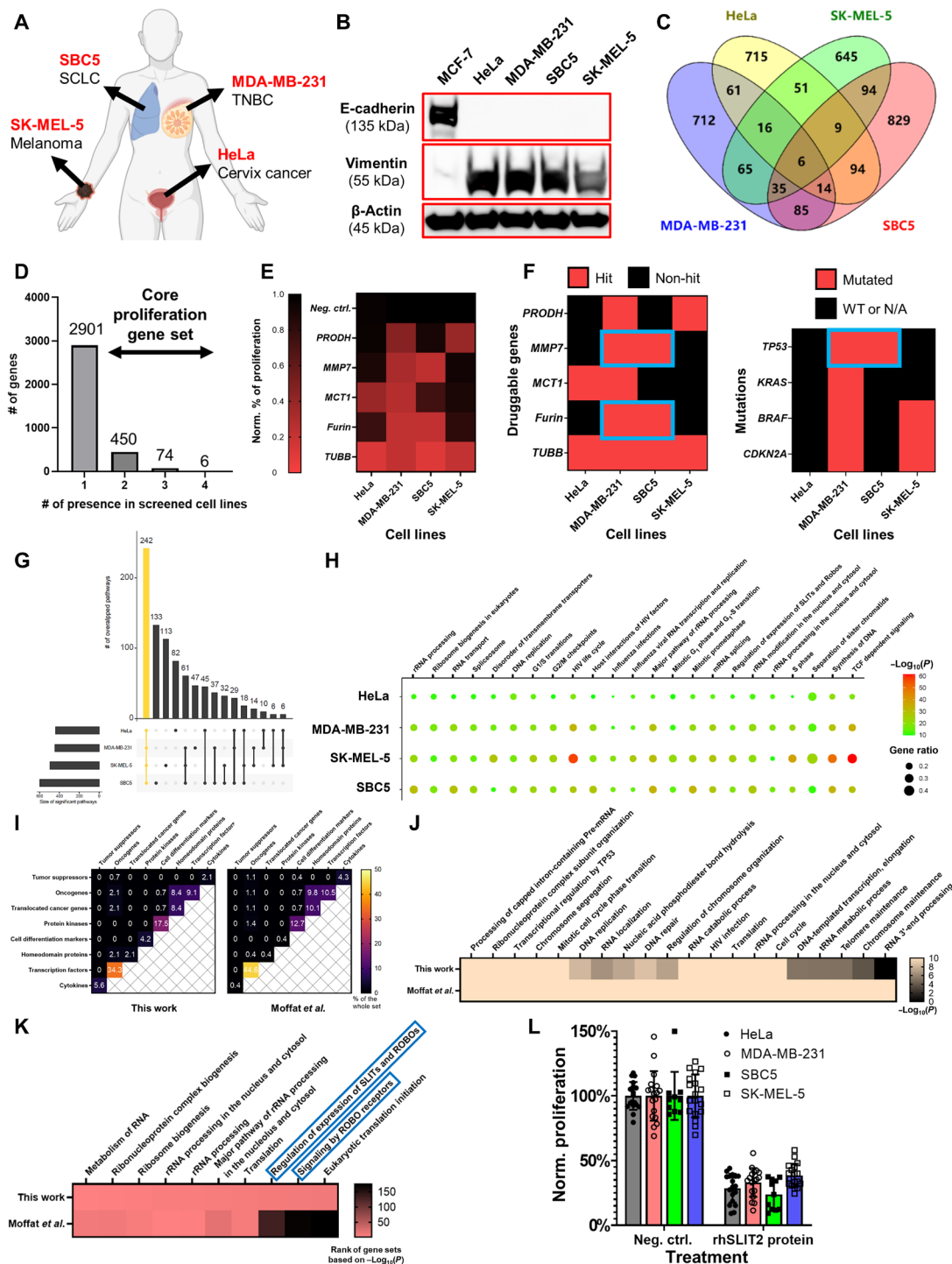
Fig. 4. Identification of proliferation landscape of mesenchymal cancer cell lines using the NanoPro assay. (**A**) Schematics showing the origin of the mesenchymal panel of cancer cell lines. (**B**) Western blot results of vimentin and E-cadherin to confirm the mesenchymal phenotypes of the panel. (**C**) Venn diagram showing the overlap of hits from each cell line. (**D**) Definition of the core proliferation gene sets; a hit shows up multiple times on the screen panel. (**E**) Validation of cell line–specific genes for proliferation through protein inhibitors. (**F**) Correlation between hot mutations and dependency of specific genes for proliferation. Blue square highlights the potential dependency on Furin/MMP7 signaling for *TP53*-mutant cells. WT, wild type; N/A, not applicable. (**G**) Upset plots of the enriched pathways from cell-specific genes of proliferation. Most of the enriched pathways were common and shared among all screened cell lines. (**H**) Multivariable heatmap showing the cell-specific enrichment in shared common pathways of proliferation. (**I**) Comparison of gene family between the core gene sets from this work and a previous work by Moffat and co-workers (*11*). A similar signature was observed. (**J**) Comparison of the enrichment of common pathways in two gene sets. (**K**) Comparison of the order of top pathways from this work in previous core gene sets. SLIT/ROBO pathway was not enriched in previous gene sets. (**L**) Validation of the SLIT/ROBO pathway as a general pathway to inhibit the growth of mesenchymal tumors in vitro.

high-dimensional information (Fig. 4, I to K). It is noteworthy that a previous study has reported a core proliferation gene set using epithelial cell lines and an outgrow-based approach (*11*), defined as the Moffat set below. Therefore, we sought to compare the similarity and differences between the datasets. We observed a similar distribution of the gene family from the two sets using the latest list available from gene set enrichment analysis (Fig. 4I). Over 30% of the genes reported in both sets are oncogenic transcriptional factors. ORA on both sets also reveals a similar profile of enriched pathways (Fig. 4J), including RNA processing and cell cycle. For some pathways, our set has a lower level of enrichment, indicating that the mesenchymal cancer cells may have less dependency on them for proliferation; this matches well with their ability to survive and establish secondary tumors (*58*). We also identified the SLIT/ROBO pathway as one that was higher ranked in our set compared to the Moffat set (Fig. 4K). The dramatic enrichment of SLIT/ROBO pathway using cell-specific genes and shared core sets strongly suggests their common but important role in regulating the proliferation of mesenchymal cancer cells. We recently observed that the deletion of *SLIT2* genes substantially enhances the progression of prostate cancer cells with mesenchymal phenotypes in xenograft mice (*59*). Meanwhile, prior studies suggest that the activation or overexpression of *SLIT2* attenuates the proliferation of breast cancer (*60*) and squamous cell carcinomas (*61*).

To probe the role of SLIT/ROBO signaling, we treated all cell lines with recombinant human SLIT2 proteins to activate the SLIT/ROBO pathway and observed a decrease of 50% in proliferation rate for all mesenchymal cell lines (Fig. 4L). This suggests that the SLIT/ROBO pathway may be a therapeutic target for pan-mesenchymal cancer cells, in addition to its known antitumor effects reported in epithelial cancer cell lines (*62*). Together, the comprehensive analysis of NanoPro-derived screen data broadens the applicability of targeting SLIT/ROBO pathway for attenuating the proliferation of mesenchymal cancer cells. This further validates the utility of NanoPro assay for the discovery of therapeutic targets.

DISCUSSION

At present, fewer than 5% of the cell lines listed in DepMap portal (https://depmap.org/portal/) have CRISPR knockout screening data available. One factor that contributes to this is due to the prolonged culture period and labor-extensive workflow of viability-based CRISPR screens. Active sorting of subpopulations of interest would greatly enrich the corresponding sgRNAs and significantly accelerate the screening process (*14*). However, current genome-wide CRISPR libraries contains 50,000 to 200,000 sgRNAs (*11*, *63*, *64*) to cover over 18,000 protein-encoding genes. It is empirically suggested to have at least 1000-fold representation of each guide (*52*, *65*); this requires a population of 5,000,000 to 20,000,000 cells for one replicate. Unfortunately, FACS can maximally process 3,600,000 input cells when assuming a sorting rate of 1000 cells per second. Fifty to seventy percent to of the input would be lost during the cells due to bad droplet formation or incorrect scanning (*16*, *17*). Hence, it is neither fast nor cost-effective to use FACS to sort desired populations from a CRISPR screen. MICS offers sufficient throughput but can only be applied to immuno-magnetically labeled protein markers (*15*); therefore, it is not applicable to the complex phenotypic screen that cannot be read out by a single protein marker.

The NanoPro assay described here provides a rapid, high-throughput means to generate magnetic gradients with a single-cell resolution based on cell proliferation and therefore enables the usage of MICS for profiling cell proliferation. With the combination of NanoPro and MICS, we are able to perform four parallelized CRISPR screens in 1 week, surpassing the throughput of the traditional outgrowth-based screen by an order of magnitude (four cell lines in 1 week versus one cell line in 3 to 4 weeks). The high throughput does not sacrifice the screen performance, as about 80% of the hits from the outgrowth-based screen can be successfully identified in the NanoPro/MICS workflow. Hence, we believe that the NanoPro/MICS approach would be a useful alternative compared to the outgrowth-based approach for screening the dependency of cancer proliferation. The fast turnaround of the NanoPro/MICS approach makes it more straightforward to run a dependency screen on patient-derived cancer cells for individualized treatment (*66*). In addition, the high purity and gentleness of the NanoPro/MICS approach would allow easy integration of the current workflow with existing microfluidic multi-omic pipelines (*67–71*) for in-depth phenotyping.

In addition, the proliferation of therapeutic cells is essential for the success of cell therapy, such as the induced pluripotent stem cells (iPSC)–based tissue regeneration (*72*), the persistence of chimeric antigen receptor T therapy (*73*), and the expansion of tumor-infiltrating lymphocytes targeting solid tumors (*74*, *75*). Our data suggest that T cells are compatible with the NanoPro labeling procedure (fig. S2). In addition to end-point analysis, our device supports the further subculturing of sorted cells, which may aid in selecting and preserving highly proliferative clones of iPSCs and T cells for research and manufacturing applications. Therefore, we anticipate that incorporating the NanoPro/MICS workflow would also help to accelerate the discovery of the regulator of proliferation in therapeutic cells to maximize their potency.

One technical challenge for the broad utilization of the NanoPro/MICS assay is that the sorting parameters (e.g., flow rate) need to be determined empirically. In this work, we have found that a flow rate of 5 ml/hour is effective for adherent, large cancer cell lines with diameters of 15 to 20 μm. The optimal parameter for sorting smaller and/or non-adherent cells with lower uptake capability remains to be determined. For these cells, we suggest to evaluate the sorting performance at different flow rates (e.g., at 2.5 or 7.5 ml/hour) and determine the optimal flow rate using a median fluorescence intensity (MFI)–based protocol that we previously published (*18*). Additionally, the current MICS device contains only four capture zones, which may be insufficient to capture the proliferation of fast-dividing cells, such as activated T cells. Future developments should include adding more capture zones to the platform to better capture the kinetics of these fast-dividing cells.

Together, our studies highlight the usefulness of nanoparticle-based CRISPR proliferation screening to generate datasets describing genotype-to-phenotype relationships. The throughput and resolution of NanoPro/MICS provide a means to accelerate screening for proliferation modulators, generate valuable information for downstream data-driven analysis, and facilitate the discovery of potential therapeutic targets rapidly and cost-effectively. Given its long-term stability (>11 days), it might also be feasible to extend the application of NanoPro to other cell tracking uses, such as in vivo magnetic tracking and in vivo CRISPR screens. These possibilities will be explored in our future studies.

MATERIALS AND METHODS

Fabrication and operation of microfluidic chip
Microfluidic chip for cell sorting was 3D-printed by a stereolithographic 3D printer (Microfluidics Edition 3D Printer, Creative CADworks, Toronto, Canada) using the CCW master mold for polydimethylsiloxane resin (Resinworks3D, Toronto, Canada) with a layer thickness of 25 μm as described before (37, 76). Before use, the chip was conditioned by 1% Pluronic F68 (24040032, Thermo Fisher Scientific, Waltham, MA) in phosphate-buffered saline (PBS; Wisent Bioproducts, Montreal, Canada) for 1 hour to reduce nonspecific binding between cells and chips. During experiments, each device was sandwiched by arrayed N52 NdFeB magnets (D14-N52, K&J Magnetics, Pipersville, PA) and connected to a digital syringe pump (Fusion 100, Chemyx, Stafford, TX) for fluidic processing.

Numerical simulation
Numerical simulation of the flow velocity pattern within microfluidic device was carried out by COMSOL Multiphysics (version 5.3, COMSOL Inc., Stockholm, Sweden) using a 3D creeping flow module. The key parameters were defined as follows: wall condition: no slip; boundary condition: pressure of 0 Pa with suppression of backflow, mesh size: physics-controlled, normal and inlet velocity rate: 1 mm/s.

Cell culture
MDA-MB-231 (RRID: CVCL_0062), MDA-MB-436 (RRID: CVCL_0623), and MDA-MB-453 (RRID: CVCL_0418) were purchased from the American Type Culture Collection (ATCC) (Manassas, VA) under the panel of triple-negative breast cancer: mesenchymal and luminal morphology. HeLa (RRID: CVCL_0030), SBC5 (RRID: CVCL_1679), SK-MEL-5 (RRID: CVCL_0527), and SH-SY5Y cells (RRID: CVCL_0019) were purchased from ATCC. MDA-MB-231, MDA-MB-436, MDA-MB-453, HeLa, SBC5, and SK-MEL-5 cells were cultured in RPMI 1640 supplied with 10% fetal bovine serum (FBS; Atlanta Biologicals, Atlanta, GA). SH-SY5Y cells were cultured in a 1:1 mixture of Eagle's minimum essential medium and F-12K medium supplied with 10% FBS. Naïve human CD4$^+$ CD45RA$^+$ T cells were purchased from STEMCELL Technologies (SCT; #70029, Vancouver, Canada) and maintained in ImmunoCult-XF T Cell Expansion Medium (#10981, SCT) supplied with human interleukin-2 (50 ng/ml) (#78036, SCT) and activated by CD3/CD28/CD2 cocktails (#10970, SCT) for 3 days every 10 to 14 days.

Nanomagnetic labeling of cell proliferation
Nanomagnetic labeling of cell proliferation (NanoPro) assay was performed using the carboxylated MNPs with a diameter of 25 to 30 nm (MP25-CA-5, Nanocs, Boston, MA) for general experiments or Cy5-conjugated MNPs with a diameter of 25 to 30 nm (MP25-S5-0.5, Nanocs) for flow cytometry. MNPs were mixed and suspended in ddH$_2$O to prepare a 100× working solution and further mixed with the culture medium before cell seeding. Cells were incubated with the MNPs for up to 24 hours. Incubated cells were rinsed three times by PBS before the complete medium change to wash the extracellular MNPs and cultured using the regular protocol indicated above.

XTT proliferation assays
The XTT proliferation assays were performed following a protocol provided by the manufacturer (https://goldbio.com/product/4029/xtt-sodium-salt). In brief, XTT sodium salt was purchased from

Gold Biotechnology (St. Louis, MO). The XTT solution was prepared by dissolving 5 mg of XTT in 4 ml of complete cell culture medium. Phenazine methosulfate (PMS; P9625) was obtained from Sigma-Aldrich (St. Louis, MO). The PMS solution was made by dissolving 3 mg of PMS in 1 ml of PBS. To prepare the detection solution, 10 μl of the PMS solution was mixed with 4 ml of XTT solution. Immediately after mixing, 50 or 200 μl of this detection solution was added to each well, depending on the well size (48 or 12 wells). The samples were incubated for 4 to 5 hours at 37°C and thoroughly shaken, and the absorbance at 450 nm was measured after incubation using a Varioskan plate reader (Thermo Fisher Scientific).

Flow cytometry and FACS
Cultured cells were trypsinized and collected through centrifugation. For CFSE, cell pellets were stained in PBS for 10 min (see table S4 for details). For NanoPro, cell pellets were treated as previously described using the MNPs conjugated with Cy5. Some samples were fixed by 4% methanol-free paraformaldehyde (PFA; 28908, Thermo Fisher Scientific) in PBS for 10 min. Some samples were fixed by 4% PFA and permeabilized by 0.5% Triton X-100 (648466, Sigma-Aldrich) for intracellular staining (e.g., Ki-67). Stained samples, together with unstained control, were examined immediately after staining by flow cytometers (Attune NxT, Thermo Fisher Scientific). At least 10,000 events were recorded for each sample. Acquired data were analyzed by FlowJo software (version 10.5.3, FlowJo LLC, Ashland, OR). For FACS, stained cells were sorted by BD FACSAria IIIu (Becton Dickinson, Franklin Lakes, NJ) or BD FACSMelody using a 100-μm nozzle by gating forward scatter/side scatter (FSC/SSC) and the fluorescein isothiocyanate (FITC) channel.

Confocal microscopy
Live cells stained by NanoPro or CFSE were incubated with live cell imaging solution (A14291DJ, Thermo Fisher Scientific) and imaged by a confocal microscope (Zeiss Axio Observer) with a 20× extra-long working distance (ELWD) lens in a temperature-controlled chamber. Images were stacked using the maximum projection function in the Zen software (Blue edition, Zeiss).

Transmission electron microscopy
Collected cell pellets were fixed by 2% glutaraldehyde in 0.1 M sodium cacodylate buffer (pH 7.3) for 2 hours at room temperature. After washing three times with the same buffer, the cells were serially dehydrated by 70% ethanol, 90% ethanol, and 100% ethanol solution at 10-min intervals. The dehydrated cells were embedded with Quetol-Spurr resin (EM0300, Sigma-Aldrich) overnight, sliced to 70- to 80-nm sections with an ultracut microtome (Ultracut RMC MT6000, Leica Microsystems), and loaded onto carbon-coated copper grids (Ted Pella). Cells were examined with a transmission electron microscope (FEI Tecnai 20, Thermo Fisher Scientific) using a 100-kV accelerating voltage.

Assessment of cell stress
The determination of relative levels of cell stress–related markers was carried out via a proteome profiler following the manufacturer's protocol (Human Phospho-Kinase Array Kit, ARY003B, R&D Systems). To develop the image, 1 ml of Chemi Reagent Mix was evenly added onto each set of membranes A and B and visualized using a Bio-Rad ChemiDoc imaging system. Integral intensities of dots

were quantified via WCIF ImageJ. Images were converted to 16-bit grayscale, inverted, and background-subtracted. Integral intensities of each spot were measured manually. Measured intensities were normalized based on the density of internal reference spots. Normalized intensities were compared to the unsorted controls to calculate the percentage of variation for each marker. Variation within 10%, 10 to 20%, and >20% was defined as minor, moderate, and severe, respectively.

Pooled CRISPR knockout screen

The Toronto KnockOut library version 3 (TKOv3) CRISPR knockout library was a gift from J. Moffat at the Department of Molecular Genetics, University of Toronto. The optimal conditions of virus titer were determined empirically for each cell line before screen using the protocol recommended by the library builder (*11*, *77*). For the actual screen, 100 million cells were infected at the optimal titer of the virus with polybrene (10 μg/ml) (TR-1003, Sigma-Aldrich) for 24 hours, which results in an MOI of 0.25 to 0.4. Infected cells were selected by 5 μg/ml (for SBC5) or 3 μg/ml (for others) puromycin (BioShop, Burlington, ON, Canada) for 48 to 72 hours. Subsequently, cells were passaged and recultured in a regular medium. This time point is defined as time point 0 (T0). Parts of T0 cells were treated by CFSE or NanoPro assay and cultured for 4 to 5 more days before FACS/MICS sorting. Sorted cells were collected and stored in a −80°C freezer before genomic DNA extraction. Genomic DNA extraction was performed using the QIAamp Blood Mini/Midi/Maxi kits (51104/51185/51194, Qiagen, Venlo, The Netherlands), depending on the number of recovered cells, according to the manufacturer's instructions. Sequencing libraries were prepared by amplifying gRNA inserts via a two-step PCR using primers that include Illumina TruSeq adaptors with i5 and I7 indices as described before (*77*). Resulting libraries were subsequently sequenced by an Illumina HiSeq2500 as described before (*11*). In brief, each read was completed with standard primers for dual indexing. The first 21 cycles were base additions without imaging. The actual 26–base pair read begins after the additional cycles and contains two index reads that begin with i7 and are followed by i5 sequence. Sequenced results were demultiplexed, trimmed, aligned, and mapped by the sequencing facility. Sequencing samples with an aligned read ratio below 70% were excluded from the bioinformatic analysis described below.

Bioinformatics

Read counts for all samples were combined in a matrix and normalized to 10 million reads per sample by dividing each read count by the sum of all read counts in the sample and then multiplying by 10 million. Fold changes and BF scores were calculated using the T0 sample as a reference through the BAGEL algorithm (version 0.91; https://github.com/hart-lab/bagel) (*51*). FDR is defined as 1 − precision. Genes were indexed by the order of BF scores. Genes with BF > 2 and FDR < 0.3 were considered effective hits, as recommended by the developer (*51*). Overrepresentation analysis (ORA) was performed by MetaScape (https://metascape.org/gp/index.html#/main/step1) using a default setting (*78*). The visualization of ORA was carried out by the eVITTA toolbox (*79*). Gene families were categorized based on the MsigDB 7.34 reference available at http://www.gsea-msigdb.org/gsea/msigdb/gene_families.jsp?ex=1. Venn diagrams were generated using Venny (version 2.1; https://bioinfogp.cnb.csic.es/tools/venny/).

Validation of hits

For the small molecule–based inhibition, the optimal concentration of each inhibitor titer was determined empirically by testing the three different concentrations based on reported IC_{50} (1× IC_{50}, 3× IC_{50}, and 10× IC_{50}). The highest concentration that allows >85% viability was chosen. The cells were treated by the corresponding small molecule for 48 or 72 hours as specified in the discussion. Table S5 provides the details of the inhibitor used in the validation. The cell number was measured through a 30-min calcein AM stain (564061, BD Biosciences, Franklin Lakes, NJ). The relative proliferation was quantified by normalizing the total relative fluorescence unit (RFU) signal of calcein AM to dimethyl sulfoxide (DMSO) control. For some experiments, samples were scanned by a fluorescence microscope (Axio Observer, Zeiss, Oberkochen, Germany) using a 5× ELWD lens.

Western blotting

Cells were lysed in the radioimmunoprecipitation assay buffer [9806, Cell Signaling Technology (CST), Danvers, MA] containing 1% SDS, complete protease inhibitor cocktail (11836170001, Roche, Basel, Switzerland), and PhosStop phosphatase inhibitor cocktail (4906837001, Roche). After the protein concentration was determined using the BCA Protein Assay Kit (23227, Thermo Fisher Scientific), the cell lysate was mixed with Bolt LDS Sample Buffer (B0007, Thermo Fisher Scientific) in the presence of 2.5% 2-mercaptoethanol and boiled at 70°C for 10 min before loading. Samples were separated on 4 to 12% bis-tris gradient gels (NW-04125BOX, Thermo Fisher Scientific) in MES SDS Running Buffer (NP0002, Thermo Fisher Scientific) at 120 V for 1 to 1.5 hours. Total protein (20 to 50 μg) was loaded to each lane. Separated proteins were transferred from gels to polyvinylidene difluoride membranes at 50 V in tris-glycine buffer containing 10% methanol for 2 hours. Membranes were blocked in tris-buffered saline with 0.1% Tween 20 (TBST) containing 5% fat-free milk for 2 hours at room temperature and probed with the respective primary antibodies overnight at 4°C. After at least three washes with TBST, membranes were incubated with anti-mouse or anti-rabbit horseradish peroxidase–conjugated secondary antibodies (7076 or 7074, CST) for 2 hours at room temperature. The band signals were developed with enhanced chemiluminescence reagents (RPN2109, GE HealthCare, Chicago, IL) and visualized by a Bio-Rad gel imaging system. Detailed information about antibodies used in Western blotting was given in table S6.

Statistical analysis

Most of the results were shown by GraphPad Prism (GraphPad Software, San Diego, CA) as an average ± SD unless specified elsewhere. Each dot represents a technical replicate. The data from BAGEL analysis were plotted in Excel (version 2016, Microsoft, Redmond, WA).

Supplementary Materials

This PDF file includes:
Figs. S1 to S8
Tables S1 to S6
Legends for data S1 and S2

Other Supplementary Material for this manuscript includes the following:
Data S1 and S2

REFERENCES AND NOTES

1. G. I. Evan, K. H. Vousden, Proliferation, cell cycle and apoptosis in cancer. *Nature* **411**, 342–348 (2001).

2. V. C. Yan, H. E. Butterfield, A. H. Poral, M. J. Yan, K. L. Yang, C. D. Pham, F. L. Muller, Why great mitotic inhibitors make poor cancer drugs. *Trends Cancer* **6**, 924–941 (2020).

3. B. A. Chabner, T. G. Roberts, Chemotherapy and the war on cancer. *Nat. Rev. Cancer* **5**, 65–72 (2005).

4. H. C. Zheng, The molecular mechanisms of chemoresistance in cancers. *Oncotarget* **8**, 59950–59964 (2017).

5. Y. G. Assaraf, A. Brozovic, A. C. Gonçalves, D. Jurkovicova, A. Linē, M. Machuqueiro, S. Saponara, A. B. Sarmento-Ribeiro, C. P. R. Xavier, M. H. Vasconcelos, The multi-factorial nature of clinical multidrug resistance in cancer. *Drug Resist. Updat.* **46**, 100645 (2019).

6. A. Palamidessi, C. Malinverno, E. Frittoli, S. Corallino, E. Barbieri, S. Sigismund, G. V. Beznoussenko, E. Martini, M. Garre, I. Ferrara, C. Tripodo, F. Ascione, E. A. Cavalcanti-Adam, Q. Li, P. P. Di Fiore, D. Parazzoli, F. Giavazzi, R. Cerbino, G. Scita, Unjamming overcomes kinetic and proliferation arrest in terminally differentiated cells and promotes collective motility of carcinoma. *Nat. Mater.* **18**, 1252–1263 (2019).

7. K. R. Fischer, A. Durrans, S. Lee, J. Sheng, F. Li, S. T. C. Wong, H. Choi, T. El Rayes, S. Ryu, J. Troeger, R. F. Schwabe, L. T. Vahdat, N. K. Altorki, V. Mittal, D. Gao, Epithelial-to-mesenchymal transition is not required for lung metastasis but contributes to chemoresistance. *Nature* **527**, 472–476 (2015).

8. X. Zheng, J. L. Carstens, J. Kim, M. Scheible, J. Kaye, H. Sugimoto, C. C. Wu, V. S. Lebleu, R. Kalluri, Epithelial-to-mesenchymal transition is dispensable for metastasis but induces chemoresistance in pancreatic cancer. *Nature* **527**, 525–530 (2015).

9. S. Acharyya, T. Oskarsson, S. Vanharanta, S. Malladi, J. Kim, P. G. Morris, K. Manova-Todorova, M. Leversha, N. Hogg, V. E. Seshan, L. Norton, E. Brogi, J. Massagué, A CXCL1 paracrine network links cancer chemoresistance and metastasis. *Cell* **150**, 165–178 (2012).

10. S. Balderston, G. Clouse, J.-J. Ripoll, G. K. Pratt, G. Gasiunas, J.-O. Bock, E. P. Bennett, K. Aran, Diversification of the CRISPR toolbox: Applications of CRISPR-Cas systems beyond genome editing. *CRISPR J.* **4**, 400–415 (2021).

11. T. Hart, M. Chandrashekhar, M. Aregger, Z. Steinhart, K. R. Brown, G. MacLeod, M. Mis, M. Zimmermann, A. Fradet-Turcotte, S. Sun, P. Mero, P. Dirks, S. Sidhu, F. P. Roth, O. S. Rissland, D. Durocher, S. Angers, J. Moffat, High-resolution CRISPR screens reveal fitness genes and genotype-specific cancer liabilities. *Cell* **163**, 1515–1526 (2015).

12. K. Han, E. E. Jeng, G. T. Hess, D. W. Morgens, A. Li, M. C. Bassik, Synergistic drug combinations for cancer identified in a CRISPR screen for pairwise genetic interactions. *Nat. Biotechnol.* **35**, 463–474 (2017).

13. K. A. Lawson, C. M. Sousa, X. Zhang, E. Kim, R. Akthar, J. J. Caumanns, Y. Yao, N. Mikolajewicz, C. Ross, K. R. Brown, A. A. Zid, Z. P. Fan, S. Hui, J. A. Krall, D. M. Simons, C. J. Slater, V. De Jesus, L. Tang, R. Singh, J. E. Goldford, S. Martin, Q. Huang, E. A. Francis, A. Habsid, R. Climie, D. Tieu, J. Wei, R. Li, A. H. Y. Tong, M. Aregger, K. S. Chan, H. Han, X. Wang, P. Mero, J. H. Brumell, A. Finelli, L. Ailles, G. Bader, G. A. Smolen, G. A. Kingsbury, T. Hart, C. Kung, J. Moffat, Functional genomic landscape of cancer-intrinsic evasion of killing by T cells. *Nature* **586**, 120–126 (2020).

14. O. Parnas, M. Jovanovic, T. M. Eisenhaure, R. H. Herbst, A. Dixit, C. J. Ye, D. Przybylski, R. J. Platt, I. Tirosh, N. E. Sanjana, O. Shalem, R. Satija, R. Raychowdhury, P. Mertins, S. A. Carr, F. Zhang, N. Hacohen, A. Regev, A genome-wide CRISPR screen in primary immune cells to dissect regulatory networks. *Cell* **162**, 675–686 (2015).

15. B. Mair, P. M. Aldridge, R. S. Atwal, D. Philpott, M. Zhang, S. N. Masud, M. Labib, A. H. Y. Tong, E. H. Sargent, S. Angers, J. Moffat, S. O. Kelley, High-throughput genome-wide phenotypic screening via immunomagnetic cell sorting. *Nat. Biomed. Eng.* **3**, 796–805 (2019).

16. S. A. Faraghat, K. F. Hoettges, M. K. Steinbach, D. R. Van Der Veen, W. J. Brackenbury, E. A. Henslee, F. H. Labeed, M. P. Hughes, High-throughput, low-loss, low-cost, and label-free cell separation using electrophysiology-activated cell enrichment. *Proc. Natl. Acad. Sci. U.S.A.* **114**, 4591–4596 (2017).

17. B. A. Sutermaster, E. M. Darling, Considerations for high-yield, high-throughput cell enrichment: Fluorescence versus magnetic sorting. *Sci. Rep.* **9**, 227 (2019).

18. Z. Wang, S. Ahmed, M. Labib, H. Wang, X. Hu, J. Wei, Y. Yao, J. Moffat, E. H. Sargent, S. O. Kelley, Efficient recovery of potent tumour-infiltrating lymphocytes through quantitative immunomagnetic cell sorting. *Nat. Biomed. Eng.* **6**, 108–117 (2022).

19. Z. Wang, S. Ahmed, M. Labib, H. Wang, L. Wu, F. Bavaghar-Zaeimi, N. Shokri, S. Blanco, S. Karim, K. Czarnecka-Kujawa, E. H. Sargent, A. J. R. McGray, M. De Perrot, S. O. Kelley, Isolation of tumour-reactive lymphocytes from peripheral blood via microfluidic immunomagnetic cell sorting. *Nat. Biomed. Eng* **7**, 1188–1203 (2023).

20. M. Labib, D. N. Philpott, Z. Wang, C. Nemr, J. B. Chen, E. H. Sargent, S. O. Kelley, Magnetic ranking cytometry: Profiling rare cells at the single-cell level. *Acc. Chem. Res.* **53**, 1445–1457 (2020).

21. M. Labib, Z. Wang, S. U. Ahmed, R. M. Mohamadi, B. Duong, B. Green, E. H. Sargent, S. O. Kelley, Tracking the expression of therapeutic protein targets in rare cells by antibody-mediated nanoparticle labelling and magnetic sorting. *Nat. Biomed. Eng.* **5**, 41–52 (2021).

22. M. Labib, R. M. Mohamadi, M. Poudineh, S. U. Ahmed, I. Ivanov, C.-L. Huang, M. Moosavi, E. H. Sargent, S. O. Kelley, Single-cell mRNA cytometry via sequence-specific nanoparticle clustering and trapping. *Nat. Chem.* **10**, 489–495 (2018).

23. Z. Wang, H. Wang, S. Lin, S. Ahmed, S. Angers, E. H. Sargent, S. O. Kelley, Nanoparticle amplification labeling for high-performance magnetic cell sorting. *Nano Lett.* **22**, 4774–4783 (2022).

24. C. R. Parish, Fluorescent dyes for lymphocyte migration and proliferation studies. *Immunol. Cell Biol.* **77**, 499–508 (1999).

25. A. B. Lyons, C. R. Parish, Determination of lymphocyte division by flow cytometry. *J. Immunol. Methods* **171**, 131–137 (1994).

26. C. H. J. Choi, L. Hao, S. P. Narayan, E. Auyeung, C. A. Mirkin, Mechanism for the endocytosis of spherical nucleic acid nanoparticle conjugates. *Proc. Natl. Acad. Sci. U.S.A.* **110**, 7625–7630 (2013).

27. C. E. Callmann, C. V. Barback, M. P. Thompson, D. J. Hall, R. F. Mattrey, N. C. Gianneschi, Therapeutic enzyme-responsive nanoparticles for targeted delivery and accumulation in tumors. *Adv. Mater.* **27**, 4611–4615 (2015).

28. J. L. Rouge, L. Hao, X. A. Wu, W. E. Briley, C. A. Mirkin, Spherical nucleic acids as a divergent platform for synthesizing RNA–nanoparticle conjugates through enzymatic ligation. *ACS Nano* **8**, 8837–8843 (2014).

29. J. A. Kim, C. Åberg, A. Salvati, K. A. Dawson, Role of cell cycle on the cellular uptake and dilution of nanoparticles in a cell population. *Nat. Nanotech.* **7**, 62–68 (2012).

30. J. Bourquin, D. Septiadi, D. Vanhecke, S. Balog, L. Steinmetz, M. Spuch-Calvar, P. Taladriz-Blanco, A. Petri-Fink, B. Rothen-Rutishauser, Reduction of nanoparticle load in cells by mitosis but not exocytosis. *ACS Nano* **13**, 7759–7770 (2019).

31. P. Falagan-Lotsch, E. M. Grzincic, C. J. Murphy, One low-dose exposure of gold nanoparticles induces long-term changes in human cells. *Proc. Natl. Acad. Sci. U.S.A.* **113**, 13318–13323 (2016).

32. P. Falagan-Lotsch, C. J. Murphy, Network-based analysis implies critical roles of microRNAs in the long-term cellular responses to gold nanoparticles. *Nanoscale* **12**, 21172–21187 (2020).

33. A. L. Martin, L. M. Bernas, B. K. Rutt, P. J. Foster, E. R. Gillies, Enhanced cell uptake of superparamagnetic iron oxide nanoparticles functionalized with dendritic guanidines. *Bioconjug. Chem.* **19**, 2375–2384 (2008).

34. Z. Wang, F. Xia, M. Labib, M. Ahmadi, H. Chen, J. Das, S. U. Ahmed, S. Angers, E. H. Sargent, S. O. Kelley, Nanostructured architectures promote the mesenchymal–epithelial transition for invasive cells. *ACS Nano* **14**, 5324–5336 (2020).

35. J. C. Charpentier, P. D. King, Mechanisms and functions of endocytosis in T cells. *Cell Commun. Signal* **19**, 92 (2021).

36. S. Feles, C. Overath, S. Reichardt, S. Diegeler, C. Schmitz, J. Kronenberg, C. Baumstark-Khan, R. Hemmersbach, C. E. Hellweg, C. Liemersdorf, Streamlining culture conditions for the neuroblastoma cell line SH-SY5Y: A prerequisite for functional studies. *MPS* **5**, 58 (2022).

37. Z. Wang, M. Gagliardi, R. M. Mohamadi, S. U. Ahmed, M. Labib, L. Zhang, S. Popescu, Y. Zhou, E. H. Sargent, G. M. Keller, S. O. Kelley, Ultrasensitive and rapid quantification of rare tumorigenic stem cells in hPSC-derived cardiomyocyte populations. *Sci. Adv.* **6**, eaay7629 (2020).

38. Y. Yan, Z. W. Lai, R. J. A. Goode, J. Cui, T. Bacic, M. M. J. Kamphuis, E. C. Nice, F. Caruso, Particles on the move: Intracellular trafficking and asymmetric mitotic partitioning of nanoporous polymer particles. *ACS Nano* **7**, 5558–5567 (2013).

39. R. Xiong, F. Joris, S. Liang, R. De Rycke, S. Lippens, J. Demeester, A. Skirtach, K. Raemdonck, U. Himmelreich, S. C. De Smedt, K. Braeckmans, Cytosolic delivery of nanolabels prevents their asymmetric inheritance and enables extended quantitative in vivo cell imaging. *Nano Lett.* **16**, 5975–5986 (2016).

40. S. Russell-Puleri, N. G. Dela Paz, D. Adams, M. Chattopadhyay, L. Cancel, E. Ebong, A. W. Orr, J. A. Frangos, J. M. Tarbell, Fluid shear stress induces upregulation of COX-2 and PGI$_2$ release in endothelial cells via a pathway involving PECAM-1, PI3K, FAK, and p38. *Am. J. Physiol. Heart Circ. Physiol.* **312**, H485–H500 (2017).

41. Q. Xu, G. Schett, C. Li, Y. Hu, G. Wick, Mechanical stress–induced heat shock protein 70 expression in vascular smooth muscle cells is regulated by rac and ras small g proteins but not mitogen-activated protein kinases. *Circ. Res.* **86**, 1122–1128 (2000).

42. B. J. Green, M. Marazzini, B. Hershey, A. Fardin, Q. Li, Z. Wang, G. Giangreco, F. Pisati, S. Marchesi, A. Disanza, E. Frittoli, E. Martini, S. Magni, G. V. Beznoussenko, C. Vernieri, R. Lobefaro, D. Parazzoli, P. Maiuri, K. Havas, M. Labib, S. Sigismund, P. P. D. Fiore, R. H. Gunby, S. O. Kelley, G. Scita, PillarX: A microfluidic device to profile circulating tumor cell clusters based on geometry, deformability, and epithelial state. *Small* **18**, e2106097 (2022).

43. I. Andrä, H. Ulrich, S. Dürr, D. Soll, L. Henkel, C. Angerpointner, J. Ritter, S. Przibilla, H. Stadler, M. Effenberger, D. H. Busch, M. Schiemann, An evaluation of T-cell functionality

after flow cytometry sorting revealed p38 MAPK activation. *Cytometry* **97**, 171–183 (2020).

44. A. Binek, D. Rojo, J. Godzien, F. J. Rupérez, V. Nuñez, I. Jorge, M. Ricote, J. Vázquez, C. Barbas, Flow cytometry has a significant impact on the cellular metabolome. *J. Proteome Res.* **18**, 169–181 (2019).

45. H.-S. Li, Y.-N. Zhou, L. Li, S.-F. Li, D. Long, X.-L. Chen, J.-B. Zhang, L. Feng, Y.-P. Li, HIF-1α protects against oxidative stress by directly targeting mitochondria. *Redox Biol.* **25**, 101109 (2019).

46. A. Guerra-Castellano, A. Díaz-Quintana, G. Pérez-Mejías, C. A. Elena-Real, K. González-Arzola, S. M. García-Mauriño, M. A. De La Rosa, I. Díaz-Moreno, Oxidative stress is tightly regulated by cytochrome *c* phosphorylation and respirasome factors in mitochondria. *Proc. Natl. Acad. Sci. U.S.A.* **115**, 7955–7960 (2018).

47. A. Y. Fu, C. Spence, A. Scherer, F. H. Arnold, S. R. Quake, A microfabricated fluorescence-activated cell sorter. *Nat. Biotechnol.* **17**, 1109–1111 (1999).

48. J. D. Adams, U. Kim, H. T. Soh, Multitarget magnetic activated cell sorter. *Proc. Natl. Acad. Sci. U.S.A.* **105**, 18165–18170 (2008).

49. T. Salafi, Y. Zhang, Y. Zhang, A review on deterministic lateral displacement for particle separation and detection. *Nano-Micro Lett.* **11**, 77 (2019).

50. M. Urbanska, H. E. Muñoz, J. Shaw Bagnall, O. Otto, S. R. Manalis, D. Di Carlo, J. Guck, A comparison of microfluidic methods for high-throughput cell deformability measurements. *Nat. Methods* **17**, 587–593 (2020).

51. T. Hart, J. Moffat, BAGEL: A computational framework for identifying essential genes from pooled library screens. *BMC Bioinformatics* **17**, 164 (2016).

52. E. L. V. Nostrand, S. A. Barnhill, A. A. Shishkin, D. A. Nelles, E. Byeon, T. Nguyen, Y. C. E. Wong, N. C. Gianneschi, G. W. Yeo, Unbiased identification of nanoparticle cell uptake mechanism via a genome-wide CRISPR/Cas9 knockout screen. bioRxiv 2020.10.08.332510 [Preprint] (2020). https://doi.org/10.1101/2020.10.08.332510.

53. E. D. Williams, D. Gao, A. Redfern, E. W. Thompson, Controversies around epithelial–mesenchymal plasticity in cancer metastasis. *Nat. Rev. Cancer* **19**, 716–732 (2019).

54. A. Dongre, R. A. Weinberg, New insights into the mechanisms of epithelial–mesenchymal transition and implications for cancer. *Nat. Rev. Mol. Cell Biol.* **20**, 69–84 (2019).

55. L. Ji, J. Xu, L. Liu, A. Amjad, K. Zhang, Q. Liu, L. Zhou, J. Xiao, X. Li, Mutant p53 promotes tumor cell malignancy by both positive and negative regulation of the transforming growth factor β (TGF-β) pathway. *J. Biol. Chem.* **290**, 11729–11740 (2015).

56. W.-H. Yu, E. Wu, Y. Li, H.-H. Hou, S. C. Yu, P.-T. Huang, W.-H. Kuo, D. Qi, C.-J. Yu, Matrix metalloprotease-7 mediates nucleolar assembly and intra-nucleolar cleaving p53 in gefitinib-resistant cancer stem cells. *iScience* **23**, 101600 (2020).

57. J. K. Heath, *Principles of Cell Proliferation* (Blackwell Science, 2001).

58. J. Fares, M. Y. Fares, H. H. Khachfe, H. A. Salhab, Y. Fares, Molecular principles of metastasis: A hallmark of cancer revisited. *Signal Transduct. Target. Ther.* **5**, 28 (2020).

59. F. Xia, Y. Ma, K. Chen, B. Duong, S. Ahmed, R. Atwal, D. Philpott, T. Ketela, J. Pantea, S. Lin, S. Angers, S. O. Kelley, Genome-wide in vivo screen of circulating tumor cells identifies *SLIT2* as a regulator of metastasis. *Sci. Adv.* **8**, eabo7792 (2022).

60. A. Prasad, V. Paruchuri, A. Preet, F. Latif, R. K. Ganju, Slit-2 induces a tumor-suppressive effect by regulating β-catenin in breast cancer cells. *J. Biol. Chem.* **283**, 26624–26633 (2008).

61. S. Srivastava, K. M. Pang, M. Iida, M. S. Nelson, J. Liu, A. Nam, J. Wang, I. Mambetsariev, R. Pillai, A. Mohanty, N. McDaniel, A. Behal, P. Kulkarni, D. L. Wheeler, R. Salgia, Activation of EPHA2-ROBO1 heterodimer by SLIT2 attenuates non-canonical signaling and proliferation in squamous cell carcinomas. *iScience* **23**, 101692 (2020).

62. R. K. Gara, S. Kumari, A. Ganju, M. M. Yallapu, M. Jaggi, S. C. Chauhan, Slit/Robo pathway: A promising therapeutic target for cancer. *Drug Discov. Today* **20**, 156–164 (2015).

63. N. E. Sanjana, O. Shalem, F. Zhang, Improved vectors and genome-wide libraries for CRISPR screening. *Nat. Methods* **11**, 783–784 (2014).

64. J. G. Doench, N. Fusi, M. Sullender, M. Hegde, E. W. Vaimberg, K. F. Donovan, I. Smith, Z. Tothova, C. Wilen, R. Orchard, H. W. Virgin, J. Listgarten, D. E. Root, Optimized sgRNA design to maximize activity and minimize off-target effects of CRISPR-Cas9. *Nat. Biotechnol.* **34**, 184–191 (2016).

65. K. Blakely, T. Ketela, J. Moffat, Pooled lentiviral shRNA screening for functional genomics in mammalian cells, in *Network Biology*, G. Cagney, A. Emili, Eds. (Humana Press, 2011), vol. 781 of *Methods in Molecular Biology*, pp. 161–182.

66. Individualized treatments for the many. *Nat. Biomed. Eng.* **3**, 755–756 (2019).

67. N. Altemose, A. Maslan, C. Rios-Martinez, A. Lai, J. A. White, A. Streets, μDamID: A microfluidic approach for joint imaging and sequencing of protein-DNA interactions in single cells. *Cell Syst.* **11**, 354–366.e9 (2020).

68. A. M. Streets, X. Zhang, C. Cao, Y. Pang, X. Wu, L. Xiong, L. Yang, Y. Fu, L. Zhao, F. Tang, Y. Huang, Microfluidic single-cell whole-transcriptome sequencing. *Proc. Natl. Acad. Sci. U.S.A.* **111**, 7048–7053 (2014).

69. P. Zhang, X. Han, J. Yao, N. Shao, K. Zhang, Y. Zhou, Y. Zu, B. Wang, L. Qin, High-throughput isolation of cell protrusions with single-cell precision for profiling subcellular gene expression. *Angew. Chem. Int. Ed.* **58**, 13700–13705 (2019).

70. P. Zhang, J. Yao, B. Wang, L. Qin, Microfluidics-based single-cell protrusion analysis for screening drugs targeting subcellular mitochondrial trafficking in cancer progression. *Anal. Chem.* **92**, 3095–3102 (2020).

71. H.-W. Lu, A. A. Kane, J. Parkinson, Y. Gao, R. Hajian, M. Heltzen, B. Goldsmith, K. Aran, The promise of graphene-based transistors for democratizing multiomics studies. *Biosens. Bioelectron.* **195**, 113605 (2022).

72. M. Ogawa, S. Ogawa, C. E. Bear, S. Ahmadi, S. Chin, B. Li, M. Grompe, G. Keller, B. M. Kamath, A. Ghanekar, Directed differentiation of cholangiocytes from human pluripotent stem cells. *Nat. Biotechnol.* **33**, 853–861 (2015).

73. J. A. Fraietta, S. F. Lacey, E. J. Orlando, I. Pruteanu-Malinici, M. Gohil, S. Lundh, A. C. Boesteanu, Y. Wang, R. S. O'Connor, W.-T. Hwang, E. Pequignot, D. E. Ambrose, C. Zhang, N. Wilcox, F. Bedoya, C. Dorfmeier, F. Chen, L. Tian, H. Parakandi, M. Gupta, R. M. Young, F. B. Johnson, I. Kulikovskaya, L. Liu, J. Xu, S. H. Kassim, M. M. Davis, B. L. Levine, N. V. Frey, D. L. Siegel, A. C. Huang, E. J. Wherry, H. Bitter, J. L. Brogdon, D. L. Porter, C. H. June, J. J. Melenhorst, Determinants of response and resistance to CD19 chimeric antigen receptor (CAR) T cell therapy of chronic lymphocytic leukemia. *Nat. Med.* **24**, 563–571 (2018).

74. M. Hall, H. Liu, M. Malafa, B. Centeno, P. J. Hodul, J. Pimiento, S. Pilon-Thomas, A. A. Sarnaik, Expansion of tumor-infiltrating lymphocytes (TIL) from human pancreatic tumors. *J. Immunother. Cancer* **4**, 61 (2016).

75. M. Poch, M. Hall, A. Joerger, K. Kodumudi, M. Beatty, P. P. Innamarato, B. L. Bunch, M. N. Fishman, J. Zhang, W. J. Sexton, J. M. Pow-Sang, S. M. Gilbert, P. E. Spiess, J. Dhillon, L. Kelley, J. Mullinax, A. A. Sarnaik, S. Pilon-Thomas, Expansion of tumor infiltrating lymphocytes (TIL) from bladder cancer. *Onco Targets Ther.* **7**, e1476816 (2018).

76. Z. Wang, E. H. Sargent, S. O. Kelley, Ultrasensitive detection and depletion of rare leukemic B cells in T cell populations via immunomagnetic cell ranking. *Anal. Chem.* **93**, 2327–2335 (2021).

77. B. Mair, J. Tomic, S. N. Masud, P. Tonge, A. Weiss, M. Usaj, A. H. Y. Tong, J. J. Kwan, K. R. Brown, E. Titus, M. Atkins, K. S. K. Chan, L. Munsie, A. Habsid, H. Han, M. Kennedy, B. Cohen, G. Keller, J. Moffat, Essential gene profiles for human pluripotent stem cells identify uncharacterized genes and substrate dependencies. *Cell Rep.* **27**, 599–615.e12 (2019).

78. Y. Zhou, B. Zhou, L. Pache, M. Chang, A. H. Khodabakhshi, O. Tanaseichuk, C. Benner, S. K. Chanda, Metascape provides a biologist-oriented resource for the analysis of systems-level datasets. *Nat. Commun.* **10**, 1523 (2019).

79. X. Cheng, J. Yan, Y. Liu, J. Wang, S. Taubert, eVITTA: A web-based visualization and inference toolbox for transcriptome analysis. *Nucleic Acids Res.* **49**, W207–W215 (2021).